

In vivo clearance of ^{19}F MRI imaging nanocarriers is strongly influenced by nanoparticle ultrastructure

Alexander H.J. Staal^{a,2}, Katrin Becker^{b,2}, Oya Tagit^{a,c}, N. Koen van Riessen^a, Olga Koshkina^{a,d}, Andor Veltien^e, Pascal Bouvain^b, Kimberley R.G. Cortenbach^a, Tom Scheenen^e, Ulrich Flögel^b, Sebastian Temme^{b,1}, Mangala Srinivas^{a,*,1}

^a Department of Tumor Immunology, Radboud Institute of Molecular Life Sciences, Radboudumc, Nijmegen, the Netherlands

^b Department of Molecular Cardiology, Experimental Cardiovascular Imaging, Heinrich-Heine-University, Düsseldorf, Germany

^c Oncode Institute, Utrecht, the Netherlands

^d Department of Physical Chemistry of Polymers, Max Planck Institute for Polymer Research, Mainz, Germany

^e Department of Radiology, Radboudumc, Nijmegen, the Netherlands

ARTICLE INFO

Keywords:

Nanoparticle
Perfluorocarbon
PFCE
 ^{19}F MRI
Clearance
Myocardial infarction
Cell tracking

ABSTRACT

Perfluorocarbons hold great promise both as imaging agents, particularly for ^{19}F MRI, and in therapy, such as oxygen delivery. ^{19}F MRI is unique in its ability to unambiguously track and quantify a tracer while maintaining anatomic context, and without the use of ionizing radiation. This is particularly well-suited for inflammation imaging and quantitative cell tracking. However, perfluorocarbons, which are best suited for imaging – like perfluoro-15-crown-5 ether (PFCE) – tend to have extremely long biological retention. Here, we showed that the use of a multi-core PLGA nanoparticle entrapping PFCE allows for a 15-fold reduction of half-life *in vivo* compared to what is reported in literature. This unexpected rapid decrease in ^{19}F signal was observed in liver, spleen and within the infarcted region after myocardial infarction and was confirmed by whole body NMR spectroscopy. We demonstrate that the fast clearance is due to disassembly of the ~200 nm nanoparticle into ~30 nm domains that remain soluble and are cleared quickly. We show here that the nanoparticle ultrastructure has a direct impact on *in vivo* clearance of its cargo i.e. allowing fast release of PFCE, and therefore also bringing the possibility of multifunctional nanoparticle-based imaging to translational imaging, therapy and diagnostics.

1. Introduction

In the recent decade, there has been much renewed interest in liquid perfluorocarbons (PFCs) as contrast agents for fluorine-19 Magnetic Resonance Imaging (^{19}F MRI) [1–3], particularly for cell tracking applications. ^{19}F MRI is of particular interest due to the possibility of combining background-free *in vivo* imaging with the precise anatomic localization capability of conventional ^1H MRI but without the use of ionizing radiation. Moreover, the ^{19}F signal can be quantified directly from the image [4]; unlike conventional contrast agents, such as gadolinium (Gd) and super paramagnetic iron oxide (SPIO), which alter the existing proton signal [5,6]. Such unique properties of ^{19}F MRI have enabled quantitative cell tracking for immunotherapy [7–11], and inflammation imaging applied to prevalent diseases such as myocardial

infarction, multiple sclerosis and rheumatoid arthritis among many others [12–17]. Despite the unique opportunities that ^{19}F MRI offers, the technique is hampered by sensitivity issues. Liquid PFCs with high fluorine density can satisfy the requirements for improved ^{19}F MRI detection sensitivity. Specifically for imaging applications, single resonance PFCs are the most attractive contrast agents as all fluorine atoms contribute to the signal and chemical shift artefacts are avoided [18]. However, these PFCs also have the longest *in vivo* half-lives, of up to 250 days [19].

Liquid PFCs are both hydrophobic and lipophobic and therefore need to be stabilized to achieve dispersibility in aqueous media as a prerequisite for their use in biological systems [20,21]. Commonly, PFC-based imaging agents are formulated as core-shell or single-core nano-emulsions (NEs) through emulsification with a lipid surfactant [12,22]

* Corresponding author.

E-mail address: mangala.srinivas@radboudumc.nl (M. Srinivas).

¹ Shared senior author.

² Authors provided equal contribution to this work.

or as single-core nanocapsules (NCs) using a biodegradable polymer as the stabilizing agent [23,24]. For instance, van Heeswijk et al. reported *in vivo* imaging of atherosclerotic plaques using a PFC nanoemulsion, and Foster and colleague used the commercially available CelSense to image macrophage infiltration into tumors [25,26]. However, a major issue with the use of PFCs is their long biological half-life. In particular, PFCs suitable for imaging, such as perfluoro-15-crown-5-ether (PFCE) and the linear perfluoropolyether (PFPE), have biological half-lives well over 100 days and show slow local clearance [27,28]. This results in two issues; the first being safety concerns associated with slow clearance, and the second being local retention, which make long-term spatio-temporal follow-up challenging. For instance, although PFC emulsions have been reported as safe for human use, clinical information on this topic is sparse and involves only short follow-up periods [29–31]. Therefore, the long biological retention times of PFCs may complicate regulatory approval of PFC-containing imaging agents, analogous to the recent concerns with gadolinium deposition [32]. In addition, the poor local mobility of PFCs results in their retention at the site of their initial accumulation. For instance, PFCE-NEs used for inflammation imaging have been shown to remain at the location of inflammation long after the inflammation has subsided [28]. A similar phenomenon was observed when tracking *ex vivo*-labelled cells, where the PFC label remained at the administration site long after the labelled cells have died [33,34]. Therefore, long-term follow-up and assessment of temporal dynamics can be a problem with long-living imaging agents, therefore there is a need for PFC imaging agents with faster *in vivo* clearance.

Polymeric carriers can provide a versatile platform for the design of imaging agents [35]. Poly (lactic-co-glycolic acid) (PLGA) is among the most commonly studied materials as carriers due to its biocompatibility, tunable degradation profile and long clinical history for various applications [36–40]. We previously reported the encapsulation of PFCE in PLGA nanoparticles (NPs), and demonstrated their applications in multi-modal imaging of therapeutic cells [41–46]. A detailed structural characterization of these NPs revealed the presence of multiple, distinct PFCE domains stabilized by the polymeric matrix as a multi-core NP [47]. In the present study, we investigate additional advantageous properties of these imaging agents in comparison to single-core alternatives formulated as NEs and NCs in terms of their *in vivo* clearance. The biological half-lives of all three formulations (NE, NC, NP) were quantitatively determined using ^{19}F MRI and were found to differ significantly depending on the formulations' ultrastructure. *In vitro* degradation analyses performed with atomic force microscopy and dynamic light scattering, as well as cell experiments supported our hypothesis that *in vivo* clearance rate strongly depends on the ultrastructure of the formulations. We further show the faster clearance of the multi-core NPs in a myocardial infarction model as a clinically applicable representative of inflammation imaging. Overall, our findings present the direct link between NP ultrastructure and their *in vivo* clearance rate. The multi-core NP can potentially satisfy the requirements of fast-clearing, highly sensitive ^{19}F MRI agents suitable for clinical imaging and diagnostics.

2. Methods

2.1. Materials

Perfluoro-15-crown-5-ether (PFCE) (Exfluor, TX, USA for the NPs and NCs or Fluorochem Ltd., Hadfield, GB for the NEs), poly (D,L-lactide-co-glycolide) (PLGA) resomer RG 502H, lactide:glycolide molar ratio 50:50 (Evonik, Germany), dichloromethane (Merck, Germany), poly (vinyl alcohol) (PVA, 80% hydrolyzed) (Sigma-Aldrich, MO, USA), indocyanine green (Akorn inc., IL, USA), Carboxy Atto647 N (Atto-tec, Germany), Phosphate buffered saline (PBS) (Braun, Germany), Dichloromethane (DCM) (VWR, the Netherlands), Poly (propylene oxide) (PPO) (Sigma Aldrich, MO, USA). Phosphate buffer, Glycerol

both from Carl Roth GmbH und Co. KG, Karlsruhe, Germany.

2.2. Synthesis of multicore nanoparticles

The synthesis is previously described [44]. In short, a triphase mini-emulsion synthesis technique was used; structure formula of the main components is shown in Fig. S9. Organic phase consisted of 100 mg of PLGA and 0.5 mg of indocyanine green or 0.05 mg of Atto647 dissolved in 3 mL of dichloromethane with the addition of PPO, fluoruous phase consisted of 900 μL PFCE, aqueous phase consisted of 1.96% (wt/wt) PVA surfactant in ultrapure water. The organic phase and fluoruous phase were premixed by agitation in a Pasteur's pipet and was immediately added to 25 mL of the aqueous phase and emulsified for 3 min with the use of a Branson S250 probe sonicator (Branson Sonic Power, CT, USA) at 40% amplitude. The solvent was evaporated overnight at 4 °C. Next, the particles were collected by centrifugation, washed 4 times with deionized water, and then freeze-dried.

2.3. Synthesis of core-shell nanoemulsions

PFC particles are produced as described elsewhere; structure formula of the main components is shown in Fig. S9 [48]. In brief, 0.24% (bNE) or 2.4% (sNE) (w/w) phospholipid (Lipoid E80S, Lipoid GmbH, Ludwigshafen, Germany) is dissolved in 10 mM phosphate buffer (7 mM Na_2HPO_4 , 3 mM NaH_2PO_4 , pH 7.4 isotonicized with 2.5% (w/w) Glycerol) and pre-emulsified for 30 min on a stirrer (IKA-Werke GmbH & Co. KG, Staufen, Germany). Afterwards, 10% (w/w) perfluoro-15-crown-5 ether and 0.0025 mol% Cy5-labelled phosphatidylethanolamine (Avanti Polar Lipids Inc., Alabaster, USA), are added, again followed by a 30 min period of stirring in the dark. Thereafter, a crude emulsion is formed by high shear mixing (Ultra Turrax TP 18/10, IKA-Werke GmbH & Co. KG, Staufen, Germany). The final emulsion is produced by high shear homogenization over 10 cycles at 1000 bar, using an M – 110P Microfluidizer (Microfluidics International Corporation, Westerwood, USA). PFCs are heat-sterilized in glass vials (VWR, Radnor, USA) under standard conditions (121 °C, 1 bar, 22 min; HMC Europe GmbH, Tüßling, Germany).

2.4. Synthesis of core-shell nanocapsules

Nanocapsules were synthesized using an adapted NP synthesis protocol. An identical primary emulsion, consisting of PLGA, DCM and PFCE was added to the aqueous phase, however with sodium cholate (25 g, 1.5 % wt/wt) as surfactant. This mixture was sonicated as before. Overnight the solvent was evaporated. Subsequently, the surfactant was exchanged to PVA (10 g of 1.96 % wt/wt) by stirring at 4 °C for 5 d. After washing, the NCs were freeze-dried.

2.5. Imaging agent characterization

Hydrodynamic radius was measured with DLS experiments performed on a Malvern Zetasizer ZS Nano (Malvern, United Kingdom). Samples were measured at a concentration of 0.01 mg/mL in a disposable cuvette.

PFCE content of NPs and NEs was measured with NMR experiments performed on a 9.4 T Bruker Avance III 400 MHz instrument, equipped with a BBFO-probe. NPs or NCs were dissolved in D_2O (Sigma Aldrich, Germany) and a 1% TFA (Trifluoroacetic acid) (Sigma Aldrich, Germany) internal reference was added. The mixture was measured at –85 ppm with a sweep width of 40 ppm and 8 averages with an interscan delay of 25 s. Data was analyzed with Mestrenova 10.0.2.

Particles were analyzed on a ζ -Sizer (Microtrac GmbH, Krefeld, Germany), run with Microtrac FLEX 10.5.0 Software (Microtrac GmbH, Krefeld, Germany). For this purpose, 20 μL of the respective substance were mixed with 1 mL ddH_2O . A measurement protocol was used which consisted of 10 cycles, 90 s each.

2.6. *In vivo* biodistribution and clearance experiments

8-14-week-old wild type C57Bl/6 male and female mice were purchased from Charles River Laboratory, Germany and maintained under specific pathogen-free conditions, received *ad libitum* standard mouse chow diet and tap water, in the Central Animal Laboratory in Nijmegen, the Netherlands and the Zentrale Einrichtung für Tierforschung und wissenschaftliche Tierschutzaufgaben (ZETT) in Düsseldorf, Germany. All animal experiments in Nijmegen were conducted in accordance to the guidelines for animal care of the Nijmegen Animal Experiments committee under Central Committee of Animal experiments permit (AVD1030020173444). All animal experiments in Düsseldorf were conducted in accordance to the EU Directive 2010/63/EU on the protection of animals used for scientific purposes (Landesamt für Natur, Umwelt und Verbraucherschutz (LANUV) Nordrhein – Westfalen, Recklinghausen, Germany; AZ 81–02.04.2018. A007).

At the start of the NP and 90 nm and 200 nm NE clearance experiments, 56 mice were injected in the tail vein with 20 mg of NPs dissolved by sonication in 0.9% NaCl or a fluorine equivalent amount of NEs. Per nanoparticle, 5 mice were imaged on day 1 after injection and subsequently sacrificed, 6 mice were imaged at timepoints 1, 3, 6 and 24 h, 6 mice were imaged at timepoints 4, 7, 14, 21 and 28 days and additional 5 mice were imaged at timepoints 2 h and 2, 4, 7 and 14 days, after which they were sacrificed.

To assess NC clearance, 5 mice were injected in the tail vein with 20 mg of NCs dissolved by vortexing in 0.9% NaCl. Mice were imaged 2 h and 2, 4, 7 and 14 days after injection, after which they were sacrificed. Liver and spleen of NP, NE and NC injected mice were collected for histology.

For the toxicity experiments mice received nanoparticles at a concentration of 100 mg/mL. Via intravenous tail vein injection three mice received 400 μ L, three mice received a total of 600 μ L in two –1 h spaced-injections and 3 control mice were not injected. Nanoparticle concentration were chosen as the highest concentration without significant increase of viscosity, injection volumes are highest volumes that do not cause volume overload. Two weeks after injection the liver and spleen were removed, fixed in 10% of formalin and snap frozen. Five μ m cryosections were cut and stained with routine hematoxylin and eosin (H&E).

During imaging, mice were anesthetized using isoflurane, 3% induction and 1.5–2% maintenance, to achieve a stable breathing rate of 60–90/minute. Core temperature was kept between 36 and 37.5 °C using an in-house build water heated mattress in Nijmegen and by heating the cooling system of the MRT to 32 °C in Düsseldorf. A reference tube, containing a homogeneous solution of the injected imaging agent diluted 1:10 in 0.9% NaCl, was placed next to the animal to allow for quantification.

2.7. Magnetic resonance imaging

Image data was recorded on a Bruker BioSpec 117/16 11.7 T MRI (Bruker, Germany) in Nijmegen and a Bruker AVANCE III 9.4 T wide-bore nuclear MR spectrometer (Bruker, Germany) in Düsseldorf, using a dual-tuned birdcage coil.

2.8. Phantom experiments

NPs were dissolved in phosphate buffered saline at concentrations of 5, 10, 15, 20, 25, 30, 40 and 50 mg/mL and sonicated thoroughly to produce a homogeneous solution and transferred to PCR tubes. A 3D RARE sequence with parameters: TR 1500 ms, TE 6.62 ms, turbo factor 44, 2 averages, matrix $64 \times 44 \times 16$, field of view of $32 \times 22 \times 32$ mm³, imaging time 48 s was used to image the phantom tubes. T1 and T2 mapping was used to determine T1 and T2 of various concentrations of NPs. T1 mapping was done using an inversion recovery sequence with a RARE readout. Parameters: 8 inversion recovery images between 300 ms

and 1400 ms, constant TR 1800 ms, TE 4.32 ms turbo factor 35, 20 averages, field of view $35 \times 35 \times 3$ mm³, voxel size $1 \times 1 \times 3$ mm, scan time 4:48 min. T2 mapping was done using a 2D RARE with 8 echo images between 50 ms and 750 ms. TR 1500 ms, TE 50–750 ms, turbo factor 2, 20 averages, field of view $35 \times 35 \times 3$ mm³, voxel size $1 \times 1 \times 3$ mm³, scan time 8:30 min.

2.9. *In vivo* mouse experiments

For ¹⁹F imaging in Nijmegen a 3D RARE sequence was used, imaging parameter: TR 1500 ms, TE 6.62 ms, turbo factor 44, 32 averages, matrix $64 \times 44 \times 16$, field of view of $32 \times 22 \times 32$ mm³, imaging time 12:48 min. Excitation frequency 470.743 MHz and an excitation bandwidth of 1 kHz to avoid isoflurane artefacts. Co-registration of ¹H anatomical images was done with a respiratory triggered unspoiled 2D FLASH, imaging parameters: TE 6 ms, TR 350 ms, FA 80 deg, 2 averages, matrix 256×256 , field of view 32×32 mm, 24 1 mm thick slices for an imaging time ~10 min depending on the respiratory rate.

For ¹⁹F imaging in Düsseldorf a RARE-sequence was used, imaging parameters: TR 2500 ms, TE 69.88 ms, 128 averages, matrix 64×64 , field of view 2.56×2.56 cm², 2 mm thick slices, 13 slices, imaging time 10:40 min, excitation frequency 376.46 MHz. Co-registration of ¹H anatomical images was done with a RARE-sequence, imaging parameters: TE 36.23 ms, TR 2500 ms, 13 averages, matrix 256×192 , field of view 2.56×2.56 cm², 2 mm thick slices, 13 slices, imaging time 2:30 min, excitation frequency 400.13 MHz. For data analysis, matrices were reconstructed to 256×256 .

To investigate bladder and gallbladder PFCE content, an adapted ¹⁹F sequence with higher detection threshold was used; single slice 2D RARE, in plane resolution 1×1 mm, 6 mm slice to cover the entire bladder, turbo factor 32, 500 averages.

2.10. Data analysis of *in vivo* ¹⁹F MRI measurements

¹⁹F signal intensity of the entire liver and spleen was determined *in vivo* to allow for longitudinal follow-up of the imaging probe. Follow-up of individual animals decreased data variance otherwise induced by individual anatomical differences or exact injection volume. When reporting the longitudinal follow-up of the probes, the ¹⁹F signal for each individual animal at timepoint 3 h was set as 100% and all other time-points were reported relative to 3 h signal.

Offline data analysis in Düsseldorf was performed using Fiji using the Bruker plugin. Regions of interest (ROIs) were drawn over the liver, spleen and a background region in one corner of the image of all slices containing the liver or spleen. For the liver and spleen, signal-to-noise ratio (SNR), in arbitrary units, was calculated (sum of (mean ¹⁹F-Signal of the ROI in the respective slice – mean ¹⁹F-signal of the background ROI)/means standard deviation of the background ROI). Data analysis in Nijmegen was performed using OsiriX viewer (Pixmeo SARL, Switzerland). Regions of interest were drawn over the liver, spleen, background region in one corner of the image and reference tube, and reconstructed into volumes of interest. The liver and spleen signal were corrected to the reference tube and the background signal was subtracted.

Imaging agent biodistribution was measured using *in vivo* ¹⁹F MRI of animals injected with 20 mg of NP or NC or a fluorine-equivalent amount of NE or sNE. ¹⁹F-containing organs were segmented into volumes of interest, these organs were liver, spleen, bone marrow and intra-abdominal lymph nodes. From this organ-specific signal, noise was subtracted and the signal was normalized to an internal reference tube.

2.11. *Ex vivo* ¹⁹F MRI of the liver

NPs or bNEs were injected intravenously and after 28 days, the liver was excised, washed in PBS and subsequently fixed in 4% para-formaldehyde overnight. To avoid tissue destruction due to excessive

fixation, organs were then washed again in PBS and stored in PBS at 4 °C and under light protection.

First anatomical ^1H images were obtained using a RARE-sequence with the following imaging parameters: TR 2500 ms, RARE factor 16, one average, matrix 256×192 , field of view 2.56×2.56 cm, 2 mm slice thickness, 13 slices, imaging time 0.5 min. Subsequently, ^{19}F MRI was conducted from the same field of view using a standard ^{19}F RARE sequence. Imaging parameters: TR 2500 ms, RARE factor 32, 128 averages, matrix 64×64 , field of view 2.56×2.56 cm, 2 mm slice thickness, 13 slices, imaging time ~11 min. Data analysis was performed with Fiji [49] using the MRI File Manager (Bruker) plugin [50]. Regions of interest (ROIs) were drawn to enclose the liver and a background region was placed outside the liver in the corner of the images. The signal-to-noise ratio (SNR) of the ^{19}F signal was calculated: $(\text{Mean } ^{19}\text{F-signal of the liver} - \text{mean } ^{19}\text{F-signal of the background (BKG)}) / \text{Mean standard deviation (SD) of the background ROI}$.

2.12. Nanoparticle degradation

Nanoparticles were dissolved in PBS (pH 7.4) or 2 M NaOH (pH 14) at a concentration of 10 mg/mL and kept on agitation at 750 rpm at 37 °C for 2 weeks. On day 0, 3, 7 and 13 nanoparticle size was analyzed using dynamic light scattering (DLS) on a Nanotracer Flex In-situ Analyser (Microtrac, Germany). On day 0, 1 week and 2 weeks after incubation nanoparticle size was imaged using atomic force microscopy (AFM).

Atomic force microscopy (AFM) images of nanoparticles were obtained with a Catalyst BioScope (Bruker) coupled to a confocal microscope (TCS SP5II, Leica). 100 μL of 10 mg/mL particle suspension was dried on clean glass substrates and particles were imaged in peak-force tapping mode using a silicon nitride cantilever with nominal spring constant of 0.4 N/m (Bruker). AFM images were analyzed using NanoScope analysis software (Bruker).

2.13. Cellular uptake and viability

Cultured cell lines (CHO - ECACC 85050302-, RAW264.7 - ECACC 91062702-, J774.2 - ECACC 85011428 - and THP-1 - ECACC 88081201) and primary cells (murine blood immune cells, cells isolated from murine livers and spleens) were incubated *ex vivo* with 2.5 μL NPs and 5 μL of NPs over a period of 40 (blood immune cells) or 80 min. For $^1\text{H}/^{19}\text{F}$ -MRI measurements CHO and RAW264.7 cells were incubated for 2 and 24 h. Cultured cells were cultivated under standard conditions (37 °C, 5% CO_2) in complete medium (DMEM high glucose (Merck KGaA, Darmstadt, Germany) with 10% heat-inactivated FCS (Biocrom, Berlin, Germany), 1% HEPES (Thermo Fisher Scientific Inc., Waltham, USA), 1% Sodium-Pyruvate (Thermo Fisher Scientific Inc., Waltham, USA) and 1% Penicillin/Streptomycin (Thermo Fisher Scientific Inc., Waltham, USA).

Primary cells were obtained from male C57BL/6 mice at an age of 10–14 weeks. Blood was collected from the tip of the tail of living animals. Organs were digested by collagenase II (6 mg Collagenase II - SERVA Electrophoresis GmbH, Heidelberg, Germany - and 20 μL DNase (Merck, Taufkirchen, Germany) in 4.98 mL PBS; 15 min at 37 °C on a shaker) and dissociated into single cells by passing them through a 40 μm cell strainer. Dissociation was followed by lysis of erythrocytes using in-house prepared lysis buffer (up to 5 times, 10 min on ice each) and an FcR blocking step with 1:20 FcR Blocking reagent (Miltenyi Biotec, Bergisch Gladbach, Germany) for 10 min on ice. This was followed by particle incubation at 37 °C (blood: additional incubation at 4 °C) on a shaker with sequential withdrawal of samples at 0, 5, 10, 20, 40 and 80 min.

For flow cytometry, cells were stained with the following antibodies: Blood immune cells/Spleen cells: CD45-PerCP rat anti mouse, 30-F11 (BD, Heidelberg, Germany), 1:100; CD11b-APC/Fire 750 rat anti mouse/human, M1/70 (BioLegend, San Diego, USA), 1:1000; CD3-PE/Cy7 Armenian hamster anti mouse, 145-2C11 (Biolegend, San Diego,

USA), 1:200; CD19-PE rat anti mouse, 1D3 (BD, Heidelberg, Germany), 1: 400. Liver cells: CD45-PE/Cy7 rat anti mouse, 30-F11 (BD, Heidelberg, Germany), 1:400; CD11b-APC/Fire 750 rat anti mouse/human, M1/70 (BioLegend, San Diego, USA), 1:1000; F4/80-PE rat anti mouse, BM8 (BioLegend, San Diego, USA), 1:100; CD31-PerCP Cy5.5 rat anti mouse, 390 (BioLegend, San Diego, USA), 1:200. For live-dead staining, 1 $\mu\text{g/mL}$ DAPI was used. For washing of the cells and ultimate measurements MACS-buffer (PBS with 0.5% BSA Fraktion V and 5 mM EDTA, pH 7.4) was used. Flow cytometry was performed on a FACS CantoII, run with FACSDiva software (BD Bioscience, Heidelberg, Germany), offline data analysis was performed using FlowJo software (FlowJo, LLC, Ashland, USA). To calculate the number of positive cells, the amount of Cy5/Atto647 positive cells was determined. Mortality was determined by analyzing the percentage of living cells (DAPI negative) normalized to the 0 min sample, then compared to an untreated controls.

For $^1\text{H}/^{19}\text{F}$ MRI, cells were fixed in 4% PFA (Labochem international, Heidelberg, Germany) for 10 min on ice, followed by pelleting. For quantification of the ^{19}F -signal in the pellets, a transverse section of the pellets was performed, using a RARE-sequence, imaging parameters: TR 2500 ms, TE 52.49 ms, 1024 averages, matrix 32×32 , field of view 2.56×2.56 cm², 1 mm thick slices, 12 slices, imaging time 42:40min, excitation frequency 376.46 MHz. The SNR of the pellets was calculated and different substances were compared.

2.14. Ischemia reperfusion myocardial infarction model

Wild type C57BL/6 J mice ($n = 6$), 8-12-week-old, were anaesthetized with an intraperitoneal cocktail of medetomidine, midazolam and fentanyl. Animals were intubated and mechanically ventilated. The left anterior descending coronary artery is approached via a left thoracotomy between the 3rd and 4th rib. The coronary artery was ligated for 45 min using a suture and a piece of plastic tubing, approximately 1 mm under the left atrium. When anesthetic depth became insufficient, 0.5% isoflurane was started. The ligature was removed and the thorax was closed after the 45 min of ischemia. The animals were injected with 400 μL of NPs dissolved at 100 mg/mL in PBS 3 h after waking up.

2.15. Feces NMR

Mouse feces produced between 0 and 24, 24–48 and 48–72 h after injection were collected to be investigated for PFCE content. Feces were dissolved in PBS and imaged using a 2D RARE sequence (in plane resolution 1×1 mm, 4 mm thick slices, TF 32, 512 averages). Dissolving the mouse feces in PBS did not result in a homogeneous solution, therefore MRI results might be non-representative due to line broadening or T_2 shortening. A homogeneous feces samples was prepared by putting the feces in liquid nitrogen and crushed in a mortar until a fine powder was formed. The powder was subsequently dissolved in 500 μL of D_2O by excessive sonication. An 1% TFA internal reference was added to this homogeneous feces solution and NMR was performed (8 averages with a 25 s interscan delay).

2.16. Statistics

For statistical analysis of the cell labeling and viability experiments, means and SD of individual experiments were calculated, followed by two-way ANOVA with Bonferroni post hoc analysis. Statistical analysis of the *in vivo* imaging data was done using Graphpad Prism 7 (GraphPad Software, San Diego, CA, USA). Decrease in organ signal was fitted with a 2-phase decay function. Significance of this differences was calculated with a linear regression analysis of the decrease in signal. Statistical significance of the differences between organ signal at specific time points between NPs and NEs was calculated with the Holm-Sidak method. A p-value of <0.05 was considered significant.

2.17. Data availability

The data that support the findings of this study are available from the corresponding author upon reasonable request.

3. Results

3.1. Characterization of imaging agents used

Two distinct PFCE-containing imaging agents were compared initially: core-shell or single-core lipid-based NEs and multi-core PLGA-based NPs (Fig. 1a). Dynamic light scattering (DLS) and atomic force microscopy (AFM) show that the NPs and NEs have a hydrodynamic diameter of 191 nm and 178 nm respectively, and a monodisperse size distribution (Fig. 1b and c). The lipid based NEs have a slightly more negative ζ -potential compared to the PLGA-based NPs (Table S1). MRI of NP-containing phantoms shows a highly linear ($R^2 > 0.99$) relationship between NP concentration and signal intensity, suitable for quantification of NP concentrations (Fig. S1). Additionally, a single resonance peak and a favorable T_2/T_1 relaxation time ratio indicate that these PFCE containing NPs have optimal characteristics for imaging (Fig. S1).

3.2. Only multicore NPs show significant *in vivo* clearance

We applied repeated $^1\text{H}/^{19}\text{F}$ MRI measurements to assess the biological half-life of NPs and NEs after intravenous injection in mice. A total of 32 mice divided over two academic centers were injected with 20 mg of NPs or a fluorine-equivalent amount of NEs. The animals were imaged at multiple timepoints early after injection (1 h, 3 h, 6 h or 24 h) to assess the kinetics in the liver and spleen, which are well known sites of PFC deposition [28]. In addition, we followed the ^{19}F signal in the liver and spleen over the course of five weeks to study the biological half-life of the PFCE derived ^{19}F signal. To this end, we used combined $^1\text{H}/^{19}\text{F}$ MRI to determine the signal in the blood and also in the liver and spleen. Figs. 1d and S2 shows representative sections of the liver and spleen for the NPs and NEs at various timepoints after injection. These images show that we observed strong ^{19}F signals in the liver after 3 h for both NPs (upper row) and NEs (lower). However, whereas the ^{19}F signal in the liver remained quite stable over time after injection of NE, the ^{19}F signal of the NPs showed a decrease even after day 1 which then further progressively declines over time. Quantification of the ^{19}F signal in the liver is shown in Fig. 1e where the ^{19}F MRI organ signal intensity was expressed as a percentage of the highest signal (3 h post injection). The NPs showed a significantly decreasing slope ($p = 0.0001$), the NEs did not ($p = 0.77$). After four weeks, 66% of the ^{19}F signal of the applied NEs was still present in the liver, whereas only 20% of signal from the NPs remained. Faster clearance of NP compared to NE was confirmed with *ex vivo* MRI and with whole animal *in vivo* NMR, to verify clearance of the ^{19}F signal not simply a relocation of the ^{19}F signal within the animal (Figs. S3 and S4). We also calculated the biological half-life of the ^{19}F signal for NEs and NPs, which revealed that the ^{19}F signal decay from the liver is best described by a 2-step exponential decay function (NP $R^2 = 0.84$ and NE $R^2 = 0.69$). The ^{19}F signal decay consisted of a rapid early phase (NP $t_{1/2} = 10$ h and NE $t_{1/2} = 42$ h) and a slower late phase (NP $t_{1/2} = 16$ days and NE $t_{1/2} = 100$ days). The confidence interval for the slow NE $t_{1/2}$ is very wide (43 – infinite days) and the fit is mediocre, which is in part due to the relatively short follow-up period of 28 days, and should therefore be interpreted cautiously. Interestingly, we observed that the ^{19}F signal in the spleen decreased for both imaging agents.

To investigate whether NPs also show faster local clearance from inflammatory lesions, we utilized a model of myocardial infarction. As previously described, ^{19}F MRI can be used to image inflammation by *in situ* labeling monocytes and visualizing their recruitment to an inflammatory focus [12]. Fig. 1f shows that intravenous injection of NPs 24 h after induction of myocardial infarct revealed a strong ^{19}F signal in the

area of the infarct (Fig. 1f, first panel) indicated by late Gd enhancement (LGE; Fig. 1f, fifth panel). However, over the time course of 6 days we observed a clear decrease in fluorine signal from the infarcted area (Fig. 1f, panel 2–4), which shows that the ^{19}F signal is not only released from spleen and liver but also clears from inflammatory lesions.

3.3. Ultrastructure determines the biological half-life of PFCE-NPs

To investigate the difference between NPs and NEs that may be causative for this considerably shortened biological half-life, we formulated two additional PFC-bearing imaging agents (Fig. 2). First, we investigated the effect of the surface composition and ultrastructure of the nanocarrier. For this purpose, we generated PLGA nanocapsules (NCs) with a single PFCE core (single-core PLGA-NCs; Fig. 2c) to investigate the clearance of NCs from liver and spleen. NCs were intravenously injected in mice, and the animals were imaged repeatedly over a period of 14 days. Fig. 2a and b shows that the ^{19}F signal of the NCs is not reduced but remains stable in the liver over two weeks. These results demonstrate that NCs and NEs show a similar clearance profile which is different from the NPs and indicates that the ultrastructure of nanoparticles and not the NP's surface composition is mainly responsible for the enhanced clearance rate of PFCE.

Second, we investigated the effect of nanocarrier size by formulating 90 nm sized NEs, similar to those used in previous studies with a very long half-life (Fig. 2f) [12,28,51–55]. Again, mice were injected with 90 nm NEs and clearance was tracked over a five-week period. Interestingly, these smaller NEs show the same long biological half-life as the bigger NEs (Fig. 2d and e), indicating that indicating that NEs with a size of 180 nm or 90 nm do not significantly differ in their clearance rate from the liver. However, the smaller 90 nm NEs showed substantially lower splenic and bone marrow uptake, which shows that size does influence the biodistribution of nanoformulations (Fig. S5).

3.4. Multicore NPs dissociate into smaller domains

Since we found that size, biodistribution and surface composition does not determine the biological half-life, we wondered what mechanisms would cause such rapid systemic clearance of the injected NP. The remaining key difference between the NEs and NPs is the ultrastructure since NPs have a multicore structure whereas NEs display only a single-core [47]. In contrast to PFC containing NEs, NPs consist of many domains of 24 nm PFCE droplets, each of which is stabilized by a shell of PLGA polymer, forming a single 200 nm particle [47].

To investigate whether structure influences nanoparticle degradation, we dissolved multicore NPs and core-shell NCs in physiologically buffered saline. At various time points samples were analyzed by AFM and DLS (Fig. 3a,c). Both PLGA based NPs and NCs show an initial slight increase in diameter which is due to diffusion of water into the particle that leads to swelling of the particle [56]. Interestingly, only in the multicore NPs, is this followed by disassembly into smaller domains with a hydrodynamic diameter of ~ 50 nm (Fig. 3a,c,d). These results were confirmed by AFM (Fig. 3c) which revealed large particles ($185 \text{ nm} \pm 90 \text{ nm}$) on day one and multiple smaller domains with a mean size of $30 \text{ nm} \pm 14 \text{ nm}$ after two weeks. Of note, size measured by DLS is an overestimation of the PFCE droplet size as a result of the hydrodynamic diameter being larger than the actual diameter and the remaining polymer coating. In this assay, degradation of NPs and NCs occurred through spontaneous hydrolysis and therefore took two weeks to complete. However, many *in vivo* occurring enzymes speed-up this process to occur within 24 h [39,57]. To test whether these domains contain PFCE, we performed ^{19}F MRI. PLGA domains suspended in buffer were subjected to ^{19}F MRI which revealed a homogeneous ^{19}F signal throughout the solution (Fig. 3b, left). When NPs were completely hydrolyzed by NaOH, the ^{19}F signal was shifted to the wall of the plastic tube (Fig. 3b, right). Hydrolysis of the NPs in sodium hydroxide releases the PFCE content which is not soluble in aqueous buffer and due to its

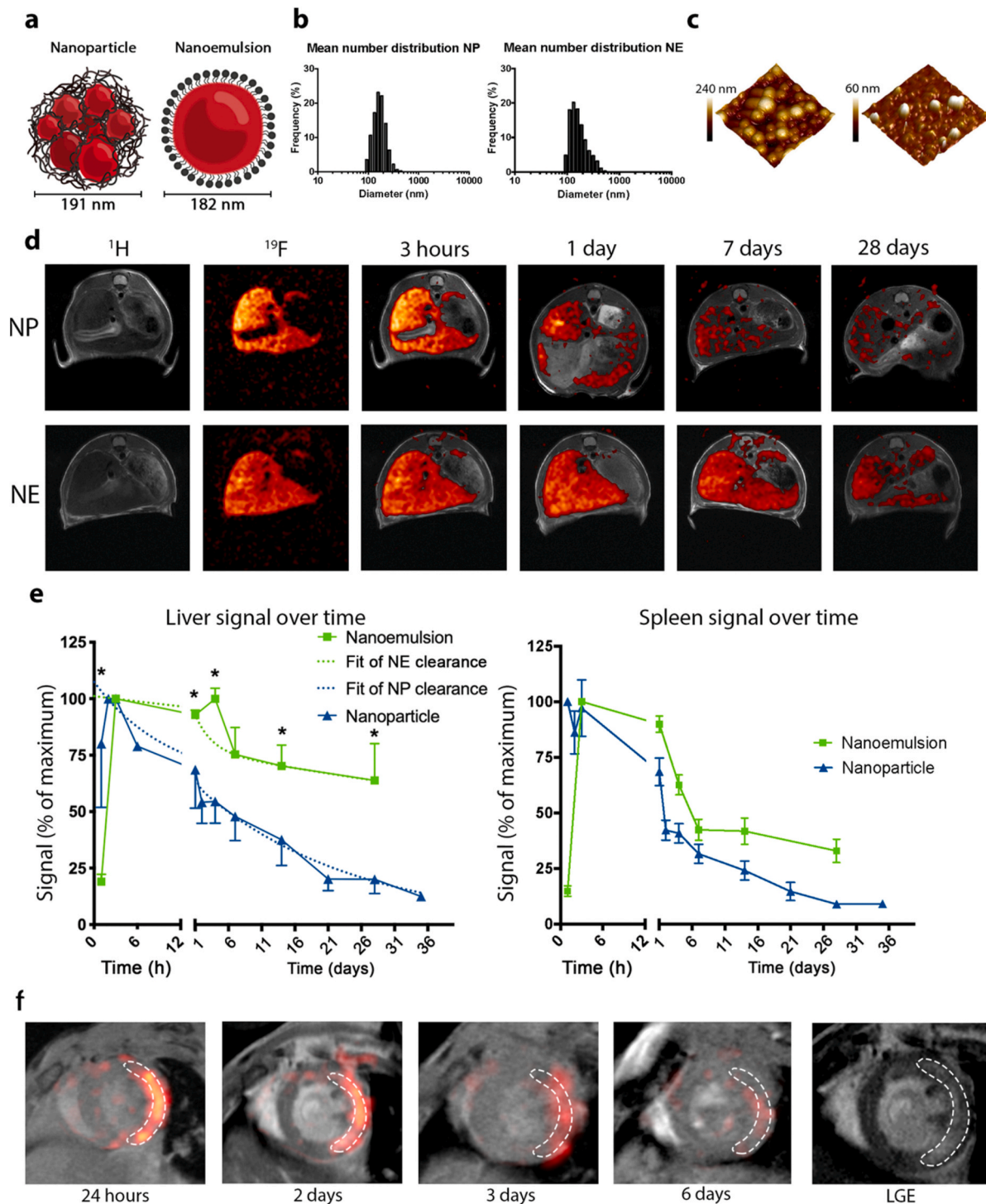


Fig. 1. Only Nanoparticles (NP) are significantly cleared over the five-week follow-up period. A total of 32 mice were injected with 20 mg of PFCE containing NPs or a fluorine-equivalent amount of NEs and repetitively scanned over a period of five weeks. **a** Illustration of the imaging agent's structure and surface composition, NP left, NE right. **b** Typical size (diameter) distribution as measured with dynamic light scattering. **c** Representative atomic force microscopy images showing size distribution of NP (left) and NE (right). Scan area $1.5 \mu\text{m} \times 1.5 \mu\text{m}$. **d** Representative transversal ^1H (greyscale) and ^{19}F (red hot) MRI images 3 h after injection to show localization of the fluorine signal in the liver, and a series of $^1\text{H}/^{19}\text{F}$ MRI images of the liver over time. The rows show NP (top) and NE (bottom) liver signal of one individual animal. **e** Liver (left) and spleen (right) ^{19}F MRI signal over time of mice injected with NPs or NEs. Signal is normalized as a percentage of the maximum signal for each individual animal over the follow-up period. Only the NPs show a significant decrease in PFCE signal over time. The dotted lines are the two-phase exponential decay fit function of the NP (green) and NE (blue) signal over time. **f** Merged mid-ventricle short axis view $^1\text{H}/^{19}\text{F}$ MRI images from a mouse injected with NPs 3 h after ischemia-reperfusion myocardial infarction of the left anterior descending coronary artery (LAD). The NPs locate to the infarcted region, visible with late gadolinium enhancement images and traced with the dashed line. Over the follow-up period of six days, decrease of the ^{19}F signal within the infarct area can be observed. Liver and bone marrow signals were masked to help image interpretation. * = $p < 0.0001$, error bars represent standard deviation. (For interpretation of the references to colour in this figure legend, the reader is referred to the Web version of this article.)

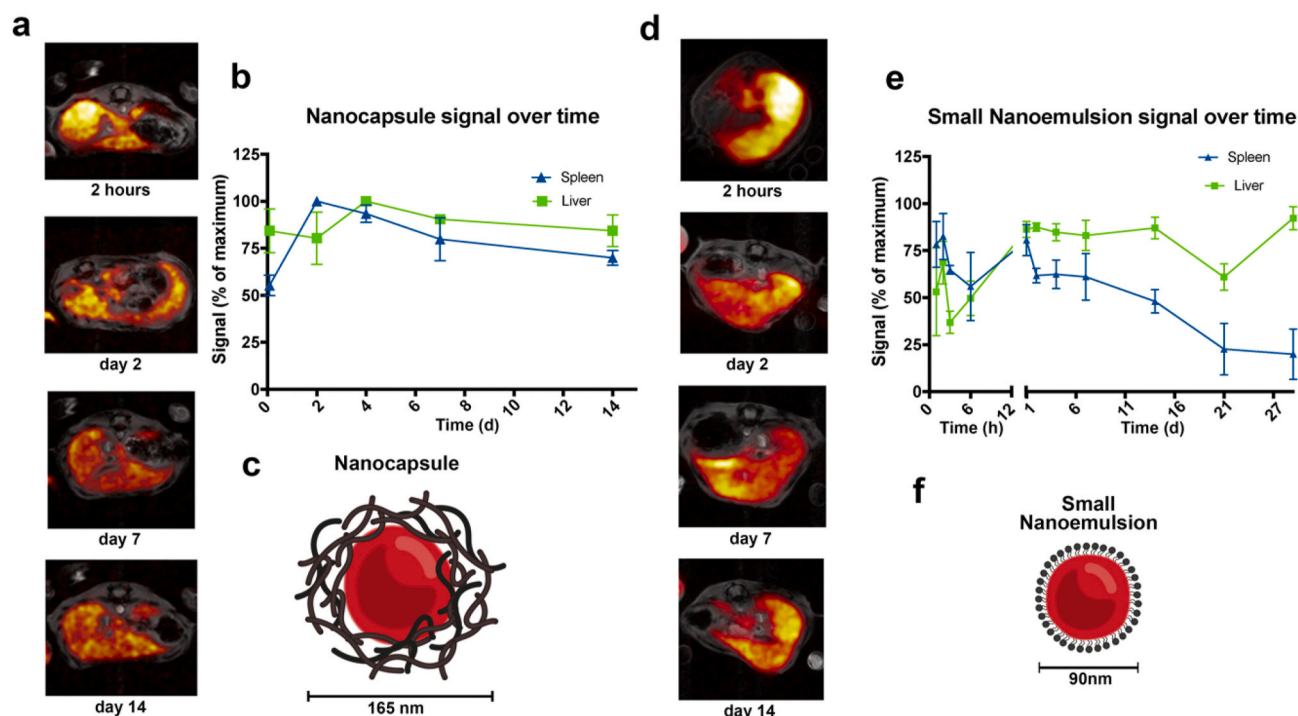


Fig. 2. Nanocarriers with a PLGA surface but a core-shell structure (nanocapsules; NC) or lipid based nanoemulsions (NE) with a smaller diameter do not show a decrease in the ^{19}F signal over time. NP clearance rate is most rapid in the first 2 weeks, longitudinal follow-up of NCs and small nanoemulsions (sNE) was chosen accordingly. **a** Representative transversal $^1\text{H}/^{19}\text{F}$ MRI images of the liver over time of animals injected with NCs. ^{19}F MRI images are in a red hot and overlaid onto grey scale ^1H MRI anatomical reference images. **b** ^{19}F MRI organ signal over time of mice injected with NCs. Signal is normalized as a percentage of the maximum signal for each individual animal over the follow-up period. Liver signal is stable over the entire follow-up duration. **c** Illustration depicting the NC with a PLGA-based core-shell structure. **d** Representative transversal $^1\text{H}/^{19}\text{F}$ MRI images of the liver over time of animals injected with sNE. ^{19}F MRI images are in a red hot and overlaid onto grey scale ^1H MRI anatomical reference images. **e** ^{19}F MRI organ signal over time of mice injected with sNE. Signal is normalized as a percentage of the maximum signal for each individual animal over the follow-up period. The spleen signal is decreasing over time. For sNEs, the liver signal remained rather stable between day 1 and day 27, except for a sharp decrease on day 21, which was probably due to artefacts such as suboptimal coil tuning, shimming, reference power correction to fluorine or positioning of the animal within the coil. **f** Illustration depicting the sNE. Error bars represent standard error of the mean. (For interpretation of the references to colour in this figure legend, the reader is referred to the Web version of this article.)

hydrophobicity sticks to the interior of the plastic tube.

Collectively, we show that multicore NPs can dissociate into smaller domains which encapsulate PFCE, which is in contrast to the single-core PFCE-nanoparticles NEs or NCs (Fig. 3d).

3.5. NPs and NCs show a stronger cellular uptake than NEs

To gain additional insight in the mechanism of the clearance we determined the cellular uptake of NPs, NCs and NEs *in vitro*. We hypothesized that NPs, NCs and NEs are taken up by cells of the reticulo-endothelial system and then are differentially degraded by these cells. Therefore, we investigated the cellular uptake of fluorescently labelled NPs, NCs and NEs by cell lines, and cells isolated from liver and spleen. Using flow cytometry, we found that NPs, NCs and NEs showed a rapid and strong cellular uptake (Figs. 4a and S6), particularly in cells isolated from liver (monocytes, neutrophils, Kupffer cells, hepatocytes). Of note, PLGA-based NPs and NCs showed a stronger fluorescence signal compared to lipid-based NEs (Fig. 4a). Similar results were observed for immune cells (monocytes, neutrophils, B- and T-cells) isolated from spleen. However, here splenic neutrophils display a lower level of uptake of NCs compared to NPs or to hepatic neutrophils. Next, we investigated by confocal microscopy if NPs and NEs are internalized into the endosomal system of the cells. To this end, we incubated CHO cells with fluorescently labelled NPs and NEs and after fixation, the cell surface was labelled by wheat germ agglutinin (WGA) and the nuclei were counterstained by DAPI. As shown in Fig. 4c, NPs and NEs can be identified as small vesicular structures in the vicinity of the nucleus. To investigate if the particles are taken up by active endocytosis, we

incubated cells with NPs, NC, and NEs at 37°C and at 4°C which blocks endocytic processes and analyzed the time-course of the labelling of the cells by flow cytometry. Interestingly, we found that cells incubated with NPs/NCs showed a rapid cellular uptake at 37°C (Fig. 4b) which is strongly reduced at 4°C . However, cells treated with NEs at 37°C or 4°C show a lower amount of cellular labelling which is only weakly ameliorated at 4°C . Taken together, this indicates that the strong uptake of the PLGA based nanoparticles is due to strong active endocytosis, which is not triggered by NEs.

Taken together, these data show that all the three nanocarriers are taken up by cells adept at degradation. Therefore, changes in cellular uptake do not explain the different systemic clearance kinetics observed between core-shell systems and multicore NPs.

3.6. PFCE encapsulated in NPs is not released via hepatic or renal routes

Finally, we explored whether the PFCE might be excreted via hepatic or renal route as an additional explanation of the increased clearance of the PFCE from the body. PFCs in general are exhaled from the lungs [20, 58, 59]. However, due to their small size and mobility the 30 nm PLGA domains might be excreted via the renal or hepatic routes. To investigate this, we performed MRI scans of the gallbladder, bladder and intestines at the timepoints at which excretion rate was highest (Figs. S7b and d). Since we expected to catch up only low amounts of PFCE, we increased the voxels size by 10-fold to enable detection of weak signals. However, no ^{19}F signal could be registered in these organs (Figs. S7b and d). Moreover, we collected all the feces which was produced within in the first 24 h after application of NPs, homogenized it with PBS to ensure

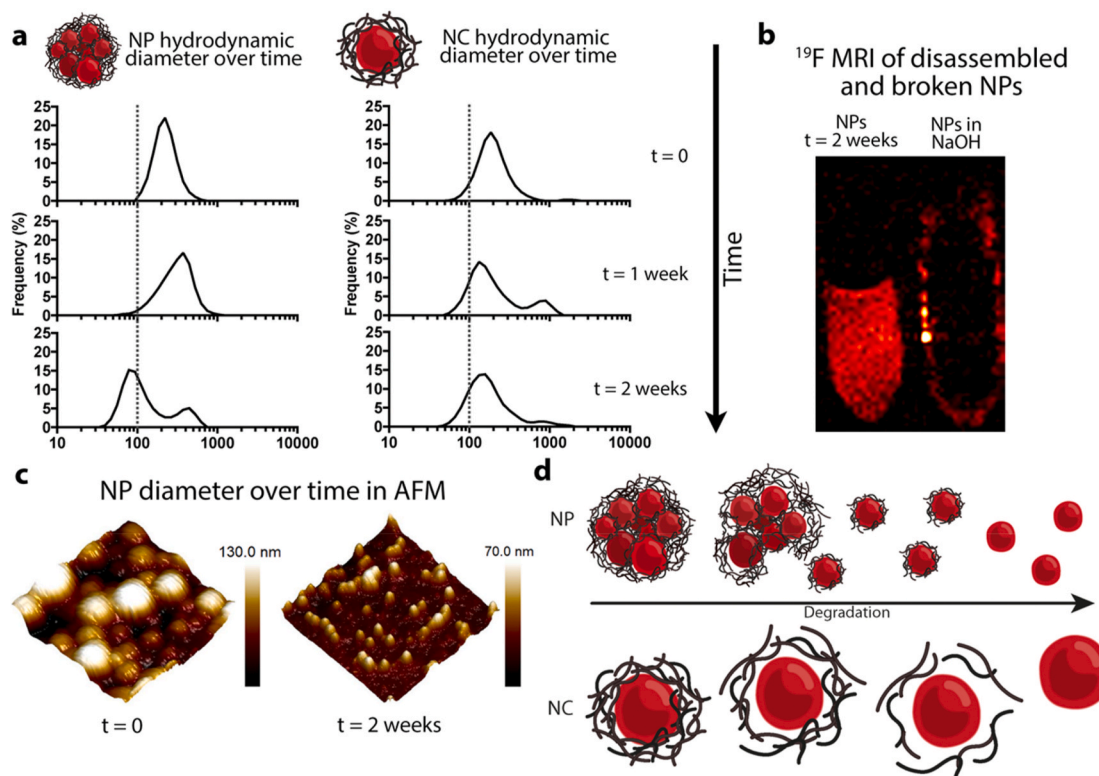


Fig. 3. Degradation of the multicore nanoparticles (NP) compared to core-shell nanocapsules (NC). **a** Size distribution in dynamic light scattering over a 2-week period, left NCs, right NPs. Both NPs and NCs show initial swelling, however only NPs show disassembly into domains after two weeks. In contrast, NCs do not degrade into smaller domains and only show minor aggregation. **b** ^{19}F MRI of NPs dissolved in phosphate buffered saline for two weeks resulting in disassembly into domains (left) and fully degraded NPs (right). Nanodomains (left) still encapsulate all PFCE as depicted by the homogeneous signal distribution in the phantom. After complete polymer degradation (right), a phase separation of the PFCE and the aqueous solution occurs which leads to a sticking of the PFCE to the plastic walls of the phantom. **c** Atomic force microscopy images showing freshly dissolved NPs (left) and the same sample after 2 weeks (right), clearly showing disassembly into nanodomains. Scan area $1\ \mu\text{m} \times 1\ \mu\text{m}$. **d** Illustration representing the different degradation patterns of NPs (top) and NCs (bottom). Note the initial swelling of NPs followed by breakdown into nanodomains. NCs also show slight swelling but do not degrade into smaller domains.

solubilization of the NPs and investigated PFCE signal by high resolution NMR-spectroscopy. However, again no traces of PFCE were found in the feces (Figs. S7a and c). An alternative possibility is that PFCE in the feces might not be stabilized by PLGA and might have condensed into pure PFCE droplets. Since PFCE has alike imaging characteristics (i.e. resonance frequency, T_1 and T_2) as PFCE in NPs, the PFCE in this state would be equally visible with MRI (Table S2). Therefore, we conclude that PFCE is not massively released via feces either as NP or pure PFCE droplet.

3.7. PFCE containing nanoparticles are biocompatible and non-toxic even at very high doses

Another aspect that is relevant to the clearance of PFC materials from the body is acute cellular toxicity, which can lead to cell death with subsequent release of NPs, followed by elimination from the body. To investigate whether clearance of the NPs might be due to increased cellular toxicity we tested cell viability by flow cytometry and also the acute and long term effects of intravenous applications of high doses of NPs/NEs to mice.

First, we isolated mouse blood, spleen and liver cells and subjected these to NEs and NPs. Cell viability over time was assessed by cytometry by DAPI staining. As shown in Fig. 5a, we did not find an increase in the amount of DAPI⁺ cells over time period of 80 min of incubation and we also found no changes in the relative abundances of individual cell types (Fig. S8). Then, we treated mice intravenously with double or triple the dose of the nanoparticles compared to the previous experiments. During the 2-week follow-up, no adverse symptoms were observed and there

was no difference in bodyweight between the groups. Histology shows no morphological changes typical for acute toxicity (Fig. 5b and c). The spleen volume did show an increase compared to the control mice, in accordance with previously reported findings for NEs [28,60,61]. In conclusion, there was no indication for short term toxicity in the mice injected with these very high NP doses. Most notably, there was no evidence of microvascular obstruction, organ toxicity or animal discomfort.

This is in accordance with previous data of these NPs, both with direct injection and after intracellular labelling in primary murine pancreatic islets, cardiac stem cells and primary human dendritic cell subsets [21,41,46,62,63].

4. Discussion

We have shown that the ultrastructure of multi-core NPs results in a unique degradation profile that results in a 15-fold faster clearance compared to conventional lipid-based and even PLGA-based single-core agents. Furthermore, cellular uptake, toxicity, biodistribution, and clearance routes are similar in all three agents.

Biological clearance is a crucially important property of an imaging agent [64,65]. Slow or non-clearance disallows the study of temporal changes (e.g. resolving inflammation or death of labelled cells) and re-use of an agent in the same animal. Furthermore, regulatory approval is difficult despite short-term non-toxicity [19,34,66], particularly given the recent issues with Gd retention [32]. In particular, single resonance PFCs such as PFCE are known to have prohibitively long *in vivo* retention times [19]. Our results with single-core nanoformulations align with

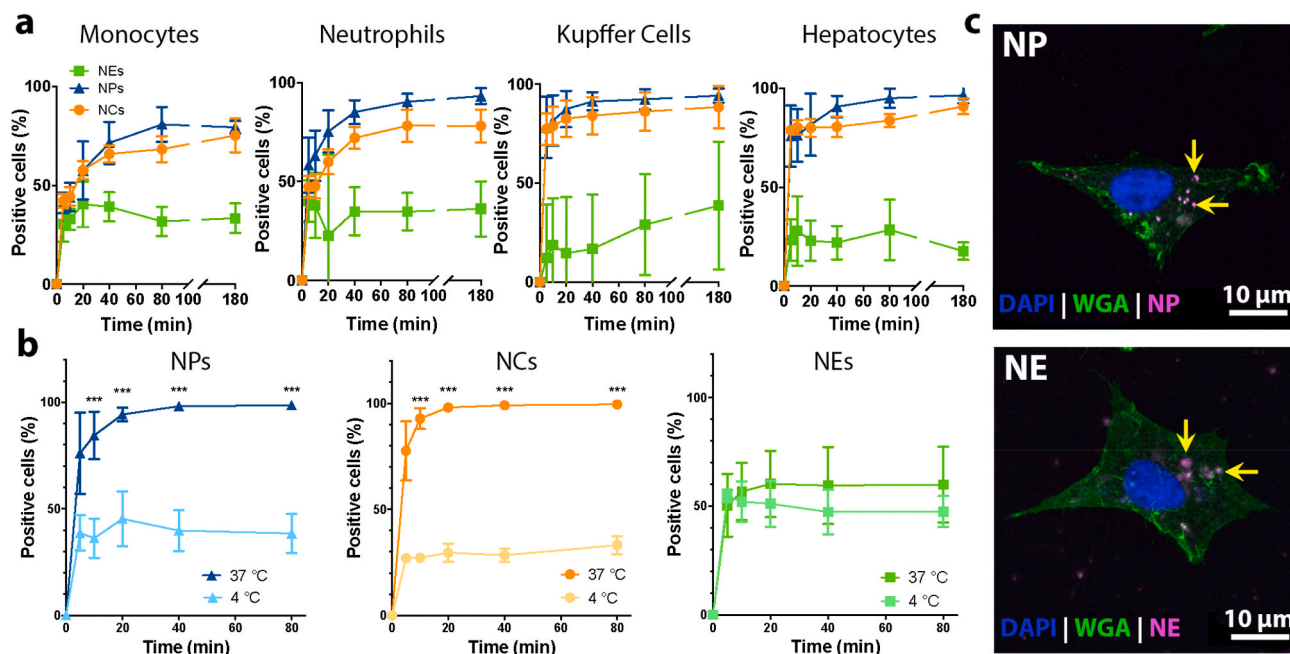


Fig. 4. *In vitro* uptake studies of PLGA-based -NP and -NC and lipid-based NE. **a** Flow cytometric analysis of monocytes, neutrophils, Kupffer cells and hepatocytes incubated with fluorescently labelled NP (blue), NC (orange) and NE (green) over a period of 180 min. Percentage of positive cells are shown as mean \pm SD for $n = 3$ individual experiments. **b** Flow cytometry analysis of RAW 264.7 cells incubated with NP, NC and NE over a period of 180 min at 37 °C and 4 °C. Percentage of positive cells are shown as mean \pm SD for $n = 5$ individual experiments. **c** Confocal microscopy images of CHO cells incubated with NPs and NEs for 90 min. The cell membrane was stained with WGA488 and the nuclei counterstained with DAPI. Arrows indicate internalized NPs and NEs labelled with Alexa647 and Cy5, respectively. The images show a merging of Alexa647/Cy5 (purple), WGA488 (green) and DAPI (blue) measurements. 400 \times magnification. (For interpretation of the references to colour in this figure legend, the reader is referred to the Web version of this article.)

previous studies. Jacoby et al. most notably conducted a study which had a follow-up duration of 80 days, this resulted in an estimated systemic PFCE half-life in excess of 250 days [19]. The biological half-life of PFCE injected as a multi-core NP is therefore extremely short at less than 1/15th of that of a single-core lipid-based NE. Thus, multi-core NPs allow the use of the PFCs best-suited for imaging, while overcoming their slow clearance.

Long local retention also hampers the clinical utility of ^{19}F MRI. When a locally accumulated tracer is not cleared, it cannot reflect resolution of inflammation or therapeutic cell viability, in inflammation imaging or cell tracking respectively. *In vivo* cell tracking using $^1\text{H}/^{19}\text{F}$ MRI holds great promise [4,11,67] as it tracks labelled cells with high specificity and excellent soft tissue resolution to show their accumulation. Moreover, imaging can also provide information regarding cell viability when the imaging agent is cleared from the region of interest when cells die. PFCE NEs have been shown to be retained at the site of cell transfer long after these cells have died therefore these labels are unable to indicate cell viability [28,66]. Here we investigate local retention in a murine model of myocardial infarction as a possible clinically applicable diagnostic application. Previously, fluorine containing imaging agents with a similar size have been used to *in situ* label immune cells [10,21,41,68]. Here we showed that monocytes and neutrophils readily take up nanoparticles *in vitro* as published previously [21]. When multi-core nanoparticles were injected intravenously, they show uptake in immune cell reservoirs like the bone marrow, spleen and liver. When an inflammatory lesion is present, these labelled cells are expected to migrate to the site of inflammation. Indeed, when we induced inflammation via a myocardial infarction model, we found strong NP accumulation in the injured region. Excitingly, we subsequently observed fast decrease of the ^{19}F signal from the infarcted region, which shows that the ^{19}F signal is not only cleared from the liver and spleen, but also from inflamed regions. This could allow for true kinetic imaging of cells *in vivo*, maintaining sensitivity to loss of cells from the region of interest. This is in keeping with our previous data

showing that multi-core NP ^{19}F signal was lost together with a luciferase reporter in transplanted pancreatic islets *in vivo* as the cells died [62].

PFCs have several unique properties, like their chemical and biological inertness which explains why PFCs such as PFCE are not metabolized *in vivo*. Endogenous pH, reactive oxygen species and enzymes do not alter or degrade the PFCE molecule. This means we can accurately track PFCE biological half-life with MRI and NMR, since PFCE is not chemically modified in a way that would change the MR resonance frequency *in vivo*. Another one of these unique features is the immiscibility of PFCs in water or fat, which is reflected in their slow clearance via the uncommon route of exhalation, and long local retention. Consequently, PFC excretion is governed by its rate of re-circulation and exhalation, this behavior is dependent on physicochemical properties specific for each PFC. Properties such as low vapor pressure and high boiling point, molecular weight and lipophobicity explain the slow clearance of PFCE. Interestingly, – to the best of our knowledge – the impact of nanoparticle structure on the biological half-life has not been studied before. Here we show for the first time how changing the ultrastructure of a nanoformulation can have relevant impact on PFCE clearing rate. We have recently described how the addition of an immiscible fluororous phase to a conventional PLGA-nanoparticle production method resulted in nano-sized particle with a unique multi-core structure [47].

Here we use DLS and AFM to show that the ultrastructure of the multi-core nanoparticle results in a unique two-step degradation pattern. First, the multi-core NP disassembles into 30 nm domains, each stabilized by their own polymer shell which keeps them dispersed in aqueous media. Based on these findings we suggest that the multi-core NP degrades into smaller PFCE-containing domains, with a larger surface area to volume ratio possibly improving re-circulation and evaporation, leading to this much faster clearance (Fig. 6). Other ways of impacting ^{19}F biological half-life is using small hydrophilic fluorinated molecules. Originally, these probes suffered from low sensitivity and toxicity but recently, tremendous progress has been made which led to

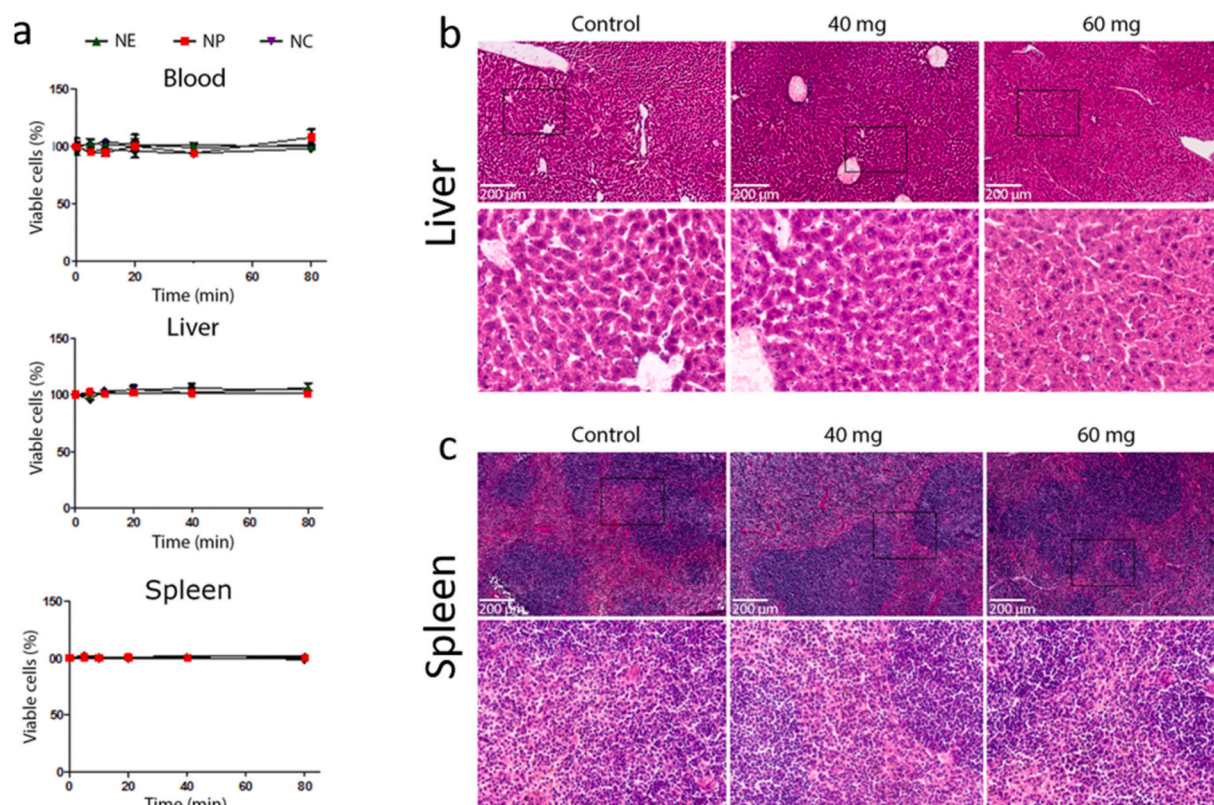


Fig. 5. The NPs, NCs and NEs do not show acute toxicity in the liver and spleen *in vivo* and relevant cells *in vitro*. Cells collected from murine blood, liver and spleen were exposed to NPs, NCs and nanoemulsions (NE) *in vitro* (a). Mice were injected with 40 mg ($n = 3$) or 60 mg ($n = 3$) of NPs and observed over a two-week period. The organs that accumulate the highest concentration of NPs, liver (b) and spleen (c), were collected after two weeks and stained with a hematoxylin and eosin stain. **a** Peripheral blood leukocytes (top) and liver (middle) and spleen (bottom) cells isolated from healthy, non-injected mice, were incubated for up to 80 min with comparable doses of NPs and NEs. At 0, 5, 10, 20, 40 and 80 min, viability was assessed with flow cytometry. Results were normalized to the $t = 0$ timepoint. **b** Liver of mice injected with 40 mg or 60 mg of NPs compared to a control mouse. Original magnification 4x (top row) and 20x (bottom row). No signs of acute liver toxicity are observed. **c** Spleen of mice injected with 40 mg or 60 mg of NPs compared to a control mouse. Original magnification 4x (top row) and 20x (bottom row). No signs of acute spleen toxicity are observed.

the development of small hydrophilic ^{19}F tracers which enabled *in vivo* imaging [69,70]. The here investigated NPs and NEs of 100–200 nm size carry a high payload of ^{19}F atoms and are avidly taken up by phagocytic cells to enable cell tracking studies. In contrast, small hydrophilic molecules might display lower uptake by phagocytic cells but might possess better tissue penetration-properties and are therefore suited for labelling of non-cellular structures like alterations in the extracellular matrix. Therefore, different types of fluorinated imaging probes have their specific advantages and drawbacks and should be selected accordingly for a particular application.

Here we solve the issues of long systemic half-life and poor local mobility, and we show how this aids translation of these NPs to the clinic in a myocardial infarct model. Additionally, these nanoparticles can be produced GMP-grade and are used to track therapeutic dendritic cells in a clinical trial (NCT02574377) [42,44,45]. The current study demonstrates the effect of the nanoparticle ultrastructure on the systemic clearance of the PFC-cargo. Formulation of a multi-core structured nanoparticle can be achieved by the addition of an inert and non-toxic fluorophilic phase to PLGA-nanoparticles, and could therefore be translatable to PLGA-nanoparticles with a drug as cargo. This finding could, thereby, introduce a new tool for control over drug delivery [44].

5. Conclusions

^{19}F MRI is an excellent, clinically-translatable candidate for quantitative inflammation imaging or cell tracking, but has been hampered by a lack of suitable agents. In particular, the extremely long clearance time

of PFCE has been a major hurdle. We have presented a PLGA-based single resonance ^{19}F -imaging agent, which is biocompatible and localizes to immune cell reservoirs of the spleen and bone marrow. Most importantly, the particles show a 15-fold faster clearance rate compared to core shell NEs, resulting in a biological half-life of 16 days, a time frame which is clinically relevant. We show how the unique multi-core ultrastructure with unique degradation profile and rapid cell uptake of these NPs causes enhanced excretion. The customizability of the multi-core PLGA formulation could also allow application to various other areas, including drug delivery and blood substitutes (the original clinical application of PFCs).

Overall, the favorable ^{19}F MRI characteristics and short biological half-life should help further implementation of PFCs in the clinic. This work shows for the first time how the ultrastructure of a PFC-containing nanoparticle can dramatically affect biological clearance.

CRediT authorship contribution statement

Alexander H.J. Staal: Methodology, Conceptualization, Investigation, Formal analysis, Writing - original draft, Visualization. **Katrin Becker:** Methodology, Conceptualization, Investigation, Formal analysis, Writing - original draft, Visualization. **Oya Tagit:** Methodology, Investigation, Formal analysis, Writing - review & editing. **N. Koen van Riessen:** Formal analysis, Investigation. **Olga Koshkina:** Investigation, Writing - review & editing. **Andor Veltien:** Methodology, Investigation. **Pascal Bouvain:** Methodology, Investigation, Formal analysis. **Kimberley R.G. Cortenbach:** Investigation, Visualization. **Tom Scheenen:**

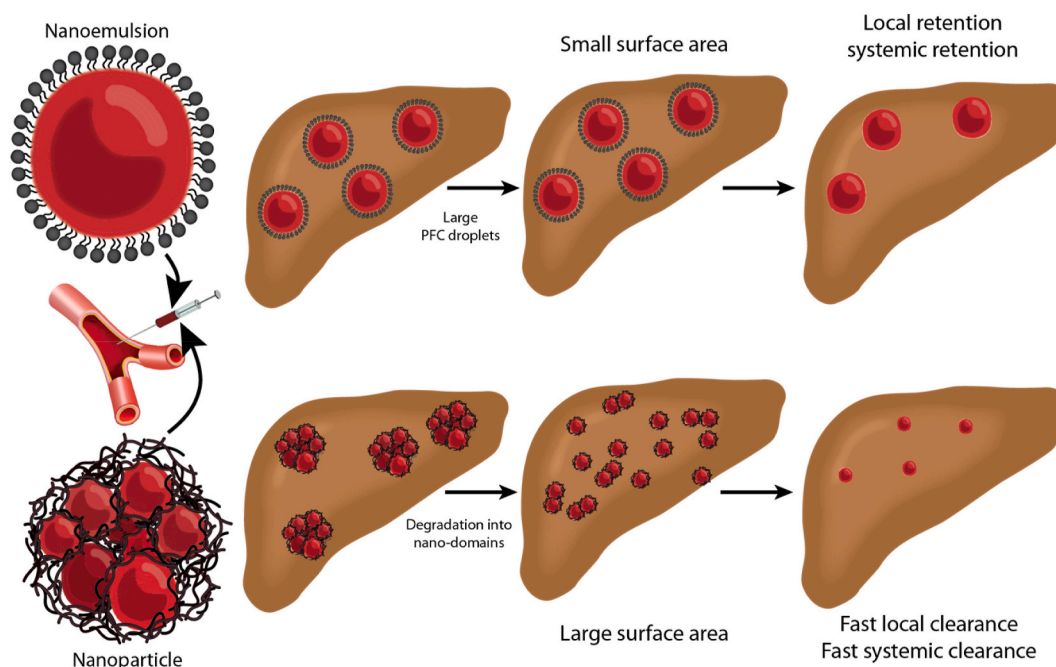


Fig. 6. Schematic illustration of how the unique ultrastructure and subsequent degradation pattern leads to an increased systemic clearance rate. Nanoemulsions (NEs) and nanoparticles (NPs) are injected intravenously after which they mainly accumulate in the liver. There, the NPs (bottom) degrade into much smaller nanodomains with a large surface area which fosters the release of PFCE and therefore enhances the clearance. The NEs (top) contain one single large PFCE core with a small surface area explaining the slower clearance.

Methodology, Supervision. **Ulrich Flögel:** Methodology, Funding acquisition. **Sebastian Temme:** Conceptualization, Writing - review & editing, Supervision, Project administration, Funding acquisition. **Mangala Srinivas:** Conceptualization, Writing - review & editing, Supervision, Project administration, Funding acquisition.

Declaration of competing interest

The authors declare the following financial interests/personal relationships which may be considered as potential competing interests: Author M.S. is a consultant to Cenya Imaging B.V., the Netherlands.

Acknowledgements

This work was funded by an ERC starting grant (ERC-2014-StG-336454-CoNQueST), TTW-NWO open technology grant (STW-14716), Deutsche Forschungsgemeinschaft grant (TE 1209/1-1, FL303/6-1 and CRC-1116), ERA-CVD grant (JTC2017-044) and two ERC Horizon 2020 Marie Skłodowska-Curie grants (MSCA-RISE-2019 'PRISAR2' and MSCA-ITN-2019 'NOVA-MRI').

We would like to thank Saskia Mulder, Kitty Lemmens, Manon Hulzen and Bianca Lemmers for performing the ischemia-reperfusion myocardial infarction surgical model or help in optimizing the surgery protocol; Bram Coolen, Gustav Strijkers and Robin Nijveldt for help with the (cardiac) MRI sequences; Edyta Swider and Roland van Kimmenade for discussions on data interpretation; Bodo Steckel for excellent technical support; Tamara Straub for help with cell culture work and flow cytometry and the center for advanced imaging (Cai) Düsseldorf for providing the confocal laser scanning microscope (Zeiss LSM 710).

Appendix A. Supplementary data

Supplementary data to this article can be found online at <https://doi.org/10.1016/j.biomaterials.2020.120307>.

References

- [1] J. Ruiz-Cabello, B.P. Barnett, P.A. Bottomley, J.W.M. Bulte, Fluorine (19F) MRS and MRI in biomedicine, *NMR Biomed.* 24 (2011) 114–129, <https://doi.org/10.1002/nbm.1570>.
- [2] J. Chen, G.M. Lanza, S.A. Wickline, Quantitative magnetic resonance fluorine imaging: today and tomorrow, *Wiley Interdiscip. Rev. Nanomedicine Nanobiotechnology.* 2 (2010) 431–440, <https://doi.org/10.1002/wnan.87>.
- [3] I. Tirotta, V. Dichiarante, C. Pigliacelli, G. Cavallo, G. Terraneo, F.B. Bombelli, P. Metrangola, G. Resnati, 19 F magnetic resonance imaging (MRI): from design of materials to clinical applications, *Chem. Rev.* 115 (2015) 1106–1129, <https://doi.org/10.1021/cr500286d>.
- [4] M. Srinivas, A. Heerschap, E.T. Ahrens, C.G. Figdor, I.J. de Vries, (19F) MRI for quantitative in vivo cell tracking, *Trends Biotechnol.* 28 (2010) 363–370, <https://doi.org/10.1016/j.tibtech.2010.04.002>.
- [5] M. Colombo, S. Carregal-Romero, M.F. Casula, L. Gutiérrez, M.P. Morales, I. B. Böhm, J.T. Heverhagen, D. Prosperi, W.J. Parak, Biological applications of magnetic nanoparticles, *Chem. Soc. Rev.* 41 (2012) 4306, <https://doi.org/10.1039/c2cs15337h>.
- [6] Y. Liu, N. Zhang, Gadolinium loaded nanoparticles in theranostic magnetic resonance imaging, *Biomaterials* 33 (2012) 5363–5375, <https://doi.org/10.1016/j.biomaterials.2012.03.084>.
- [7] E.T. Ahrens, R. Flores, H. Xu, P.A. Morel, In vivo imaging platform for tracking immunotherapeutic cells, *Nat. Biotechnol.* 23 (2005) 983–987, <https://doi.org/10.1038/nbt1121>.
- [8] E.T. Ahrens, J.W. Bulte, Tracking immune cells in vivo using magnetic resonance imaging, *Nat. Rev. Immunol.* 13 (2013) 755–763, <https://doi.org/10.1038/nri3531>.
- [9] C. Fink, M. Smith, J.M. Gaudet, A. Makela, P.J. Foster, G.A. Dekaban, Fluorine-19 cellular MRI detection of in vivo dendritic cell migration and subsequent induction of tumor antigen-specific immunotherapeutic response, *Mol. Imag. Biol.* (2019), <https://doi.org/10.1007/s11307-019-01393-8>.
- [10] C. Fink, J.M. Gaudet, M.S. Fox, S. Bhatt, S. Viswanathan, M. Smith, J. Chin, P. J. Foster, G.A. Dekaban, 19F-perfluorocarbon-labeled human peripheral blood mononuclear cells can be detected in vivo using clinical MRI parameters in a therapeutic cell setting, *Sci. Rep.* 8 (2018) 590, <https://doi.org/10.1038/s41598-017-19031-0>.
- [11] F. Chapelin, C.M. Capitini, E.T. Ahrens, Fluorine-19 MRI for detection and quantification of immune cell therapy for cancer, *J. Immunother. Cancer.* 6 (2018) 105, <https://doi.org/10.1186/s40425-018-0416-9>.
- [12] U. Flögel, Z. Ding, H. Hardung, S. Jander, G. Reichmann, C. Jacoby, R. Schubert, J. Schrader, In vivo monitoring of inflammation after cardiac and cerebral ischemia by fluorine magnetic resonance imaging, *Circulation* 118 (2008) 140–148, <https://doi.org/10.1161/CIRCULATIONAHA.107.737890>.
- [13] J. Zhong, K. Narsinh, P.A. Morel, H. Xu, E.T. Ahrens, In vivo quantification of inflammation in experimental autoimmune encephalomyelitis rats using fluorine-19 magnetic resonance imaging reveals immune cell recruitment outside the

- nervous system, *PLoS One* 10 (2015), e0140238, <https://doi.org/10.1371/journal.pone.0140238>.
- [14] H. Vu-Quang, M.S. Vinding, M. Jakobsen, P. Song, F. Dagnaes-Hansen, N. C. Nielsen, J. Kjems, Imaging rheumatoid arthritis in mice using combined near infrared and 19F magnetic resonance modalities, *Sci. Rep.* 9 (2019) 14314, <https://doi.org/10.1038/s41598-019-50043-0>.
 - [15] U. Flögel, S. Burghoff, P.L.E.M. van Lent, S. Temme, L. Galbarz, Z. Ding, A. El-Tayeb, S. Huel, F. Bönner, N. Borg, C. Jacoby, C.E. Müller, W.B. van den Berg, J. Schrader, Selective activation of adenosine A2A receptors on immune cells by a CD73-dependent prodrug suppresses joint inflammation in experimental rheumatoid arthritis, *Sci. Transl. Med.* 4 (2012), <https://doi.org/10.1126/scitranslmed.3003717>, 146ra108–146ra108.
 - [16] I.T. Ramos, M. Henningsson, M. Nezafat, B. Lavin, S. Llorio, P. Gebhardt, A. Protti, T.R. Eykyn, M.E. Andia, U. Flögel, A. Phinikaridou, A.M. Shah, R.M. Botnar, Simultaneous assessment of cardiac inflammation and extracellular matrix remodeling after myocardial infarction, *Circ. Cardiovasc. Imaging* 11 (2018), <https://doi.org/10.1161/CIRCIMAGING.117.007453>.
 - [17] R.C.I. Wüst, C. Calcagno, M.R.R. Daal, A.J. Nederveen, B.F. Coolen, G.J. Strijkers, Emerging magnetic resonance imaging techniques for atherosclerosis imaging, *Arterioscler. Thromb. Vasc. Biol.* 39 (2019) 841–849, <https://doi.org/10.1161/ATVBAHA.118.311756>.
 - [18] I.T. Ramos, E.T. Ahrens, Fluorine Magnetic Resonance Imaging, first ed., Pan Stanford Publishing Pte. Ltd., Singapore, 2016.
 - [19] C. Jacoby, S. Temme, F. Mayenfels, N. Benoit, M.P. Krafft, R. Schubert, J. Schrader, U. Flögel, Probing different perfluorocarbons for in vivo inflammation imaging by 19F MRI: image reconstruction, biological half-lives and sensitivity, *NMR Biomed.* 27 (2014) 261–271, <https://doi.org/10.1002/nbm.3059>.
 - [20] J.G. Riess, Oxygen Carriers ("Blood Substitutes")/Raison d'Etre, Chemistry, and Some Physiology Blut ist ein ganz besonderer Saft 1, *Chem. Rev.* 101 (2001) 2797–2920, <https://doi.org/10.1021/cr970143c>.
 - [21] M. Srinivas, P. Boehm-Sturm, C.G. Figdor, I.J. de Vries, M. Hoehn, Labeling cells for in vivo tracking using (19F) MRI, *Biomaterials* 33 (2012) 8830–8840, <https://doi.org/10.1016/j.biomaterials.2012.08.048>.
 - [22] J.M. Janjic, P. Shao, S. Zhang, X. Yang, S.K. Patel, M. Bai, Perfluorocarbon nanoemulsions with fluorescent, colloidal and magnetic properties, *Biomaterials* 35 (2014) 4958–4968, <https://doi.org/10.1016/j.biomaterials.2014.03.006>.
 - [23] O. Diou, N. Tsapis, C. Giraudeau, J. Valette, C. Gueutin, F. Bourasset, S. Zanna, C. Vauthier, E. Fattal, Long-circulating perfluorooctyl bromide nanocapsules for tumor imaging by 19F MRI, *Biomaterials* 33 (2012) 5593–5602, <https://doi.org/10.1016/j.biomaterials.2012.04.037>.
 - [24] E. Pisani, N. Tsapis, B. Galaz, M. Santin, R. Berti, N. Taulier, E. Kurtisovski, O. Lucidarme, M. Ourevitch, B.T. Doan, J.C. Beloeil, B. Gillet, W. Urbach, S. L. Bridal, E. Fattal, Perfluorooctyl bromide polymeric capsules as dual contrast agents for ultrasonography and magnetic resonance imaging, *Adv. Funct. Mater.* 18 (2008) 2963–2971, <https://doi.org/10.1002/adfm.200800454>.
 - [25] R.B. van Heeswijk, M. Pellegrin, U. Flögel, C. Gonzales, J.-F. Aubert, L. Mazzolai, J. Schwitler, M. Stuber, Fluorine MR imaging of inflammation in atherosclerotic plaque in vivo, *Radiology* 275 (2015) 421–429, <https://doi.org/10.1148/radiol.14141371>.
 - [26] A.V. Makela, P.J. Foster, Imaging macrophage distribution and density in mammary tumors and lung metastases using fluorine-19 MRI cell tracking, *Magn. Reson. Med.* 80 (2018) 1138–1147, <https://doi.org/10.1002/mrm.27081>.
 - [27] M.P. Krafft, J.G. Riess, Perfluorocarbons: life sciences and biomedical uses Dedicated to the memory of Professor Guy Ourisson, a true RENAISSANCE man, *J. Polym. Sci. Part A Polym. Chem.* 45 (2007) 1185–1198, <https://doi.org/10.1002/pola.21937>.
 - [28] C. Jacoby, S. Temme, F. Mayenfels, N. Benoit, M.P. Krafft, R. Schubert, J. Schrader, U. Flögel, Probing different perfluorocarbons for in vivo inflammation imaging by 19F MRI: image reconstruction, biological half-lives and sensitivity, *NMR Biomed.* 27 (2014) 261–271, <https://doi.org/10.1002/nbm.3059>.
 - [29] R.J. Noveck, E.J. Shannon, P.T. Leese, J.S. Shorr, K.E. Flaim, P.E. Keipert, C. M. Woods, Randomized safety studies of intravenous perflubron emulsion. II. Effects on immune function in healthy volunteers, *Anesth. Analg.* 91 (2000) 812–822, <https://doi.org/10.1097/0000539-200010000-00009>.
 - [30] T. Mitsuno, H. Ohyanagi, R. Naito, Clinical studies of a perfluorochemical whole blood substitute (Fluosol-DA) Summary of 186 cases, *Ann. Surg.* 195 (1982) 60, 9, <http://www.ncbi.nlm.nih.gov/pubmed/7034658>.
 - [31] R.G. Evans, B.F. Kimler, R.A. Morantz, S. Batnitzky, Lack of complications in long-term survivors after treatment with Fluosol and oxygen as an adjuvant to radiation therapy for high-grade brain tumors, *Int. J. Radiat. Oncol. Biol. Phys.* 26 (1993) 649–652, <http://www.ncbi.nlm.nih.gov/pubmed/8330996>.
 - [32] V. Gulani, F. Calamante, F.G. Shellock, E. Kanal, S.B. Reeder, Gadolinium deposition in the brain: summary of evidence and recommendations, *Lancet Neurol.* 16 (2017) 564–570, [https://doi.org/10.1016/S1474-4422\(17\)30158-8](https://doi.org/10.1016/S1474-4422(17)30158-8).
 - [33] P. Boehm-Sturm, M. Aswendt, A. Minassian, S. Michalk, L. Mengler, J. Adamczak, L. Mezzanotte, C. Löwik, M. Hoehn, A multi-modality platform to image stem cell graft survival in the naïve and stroke-damaged mouse brain, *Biomaterials* 35 (2014) 2218–2226, <https://doi.org/10.1016/j.biomaterials.2013.11.085>.
 - [34] E. Bible, F. Dell'Acqua, B. Solanky, A. Balducci, P.M. Crapo, S.F. Badyal, E. T. Ahrens, M. Modo, Non-invasive imaging of transplanted human neural stem cells and ECM scaffold remodeling in the stroke-damaged rat brain by 19F- and diffusion-MRI, *Biomaterials* 33 (2012) 2858–2871, <https://doi.org/10.1016/j.biomaterials.2011.12.033>.
 - [35] R. Thiruppathi, S. Mishra, M. Ganapathy, P. Padmanabhan, B. Gulyás, Nanoparticle functionalization and its potentials for molecular imaging, *Adv. Sci.* 4 (2017) 1600279, <https://doi.org/10.1002/advs.201600279>.
 - [36] M.C. Operti, D. Fecher, E.A.W. van Dinther, S. Grimm, R. Jaber, C.G. Figdor, O. Tagit, A comparative assessment of continuous production techniques to generate sub-micron size PLGA particles, *Int. J. Pharm.* 550 (2018) 140–148, <https://doi.org/10.1016/j.ijpharm.2018.08.044>.
 - [37] X. Li, X. Jiang, Microfluidics for producing poly (lactic-co-glycolic acid)-based pharmaceutical nanoparticles, *Adv. Drug Deliv. Rev.* 128 (2018) 101–114, <https://doi.org/10.1016/j.addr.2017.12.015>.
 - [38] S. Acharya, S.K. Sahoo, PLGA nanoparticles containing various anticancer agents and tumour delivery by EPR effect, *Adv. Drug Deliv. Rev.* 63 (2011) 170–183, <https://doi.org/10.1016/j.addr.2010.10.008>.
 - [39] E. Swider, S. Maharjan, K. Houkes, N.K. van Riessen, C. Figdor, M. Srinivas, O. Tagit, Förster resonance energy transfer-based stability assessment of PLGA nanoparticles in vitro and in vivo, *ACS Appl. Bio Mater.* 2 (2019) 1131–1140, <https://doi.org/10.1021/acsabm.8b00754>.
 - [40] M.C. Operti, Y. Dölen, J. Keulen, E.A.W. van Dinther, C.G. Figdor, O. Tagit, Microfluidics-assisted size tuning and biological evaluation of PLGA particles, *Pharmaceutics* 11 (2019) 590, <https://doi.org/10.3390/pharmaceutics11110590>.
 - [41] M. Srinivas, J. Tel, G. Schreibelt, F. Bonetto, L.-J. Cruz, H. Amiri, A. Heerschap, C. G. Figdor, I.J.M. de Vries, PLGA-encapsulated perfluorocarbon nanoparticles for simultaneous visualization of distinct cell populations by 19F MRI, *Nanomedicine* 10 (2015) 2339–2348, <https://doi.org/10.2217/nmm.15.76>.
 - [42] E. Swider, O. Koshkina, J. Tel, L.J. Cruz, I.J.M. de Vries, M. Srinivas, Customizing poly(lactic-co-glycolic acid) particles for biomedical applications, *Acta Biomater.* 73 (2018) 38–51, <https://doi.org/10.1016/j.actbio.2018.04.006>.
 - [43] M. Srinivas, L.J. Cruz, F. Bonetto, A. Heerschap, C.G. Figdor, I.J. de Vries, Customizable, multi-functional fluorocarbon nanoparticles for quantitative in vivo imaging using 19F MRI and optical imaging, *Biomaterials* 31 (2010) 7070–7077, <https://doi.org/10.1016/j.biomaterials.2010.05.069>.
 - [44] E. Swider, A.H.J. Staal, N.K. van Riessen, L. Jacobs, P.B. White, R. Fokkink, G.-J. Janssen, E. van Dinther, C.G. Figdor, I.J.M. de Vries, O. Koshkina, M. Srinivas, Design of triphasic poly(lactic-co-glycolic acid) nanoparticles containing a perfluorocarbon phase for biomedical applications, *RSC Adv.* 8 (2018) 6460–6470, <https://doi.org/10.1039/C7RA13062G>.
 - [45] E. Swider, K. Daoudi, A.H.J. Staal, O. Koshkina, N.K. van Riessen, E. van Dinther, I. J.M. de Vries, C.L. de Korte, M. Srinivas, Clinically-applicable perfluorocarbon-loaded nanoparticles for in vivo photoacoustic, 19F magnetic resonance and fluorescent imaging, *Nanotheranostics* 2 (2018) 258–268, <https://doi.org/10.7150/ntno.26208>.
 - [46] C. Constantinescu, P. Basnett, B. Lukasiewicz, R. Carnicer, E. Swider, Q.A. Majid, M. Srinivas, A.C. Carr, I. Roy, In vivo tracking and 1H/19F magnetic resonance imaging of biodegradable polyhydroxyalkanoate/polycaprolactone blend scaffolds seeded with labeled cardiac stem cells, *ACS Appl. Mater. Interfaces* 10 (2018) 25056–25068, <https://doi.org/10.1021/acsami.8b06096>.
 - [47] O. Koshkina, G. Lajoie, F. Baldelli Bombelli, E. Swider, L.J. Cruz, P.B. White, R. Schweins, Y. Dolen, E. van Dinther, N.K. van Riessen, S.E. Rogers, R. Fokkink, I. K. Voets, E.R.H. van Eck, A. Heerschap, M. Versluis, C.L. de Korte, C.G. Figdor, I.J. M. de Vries, M. Srinivas, Multicore liquid perfluorocarbon-loaded multimodal nanoparticles for stable ultrasound and 19F MRI applied to in vivo cell tracking, *Adv. Funct. Mater.* 1806485 (2019), <https://doi.org/10.1002/adfm.201806485>.
 - [48] P. Bouvain, V. Flocke, W. Krämer, R. Schubert, J. Schrader, U. Flögel, S. Temme, Dissociation of 19F and fluorescence signal upon cellular uptake of dual-contrast perfluorocarbon nanoemulsions, *Magn. Reson. Mater. Phys. Biol. Med.* 32 (2019) 133–145, <https://doi.org/10.1007/s10334-018-0723-7>.
 - [49] J. Schindelin, I. Arganda-Carreras, E. Frise, V. Kaynig, M. Longair, T. Pietzsch, S. Preibisch, C. Rueden, S. Saalfeld, B. Schmid, J.-Y. Tinevez, D.J. White, V. Hartenstein, K. Eliceiri, P. Tomancak, A. Cardona, Fiji: an open-source platform for biological-image analysis, *Nat. Methods* 9 (2012) 676–682, <https://doi.org/10.1038/nmeth.2019>.
 - [50] O. Montigon, G. Irm, INSERM, MRI File Manager (Bruker), 2015.
 - [51] B. Ebner, P. Behm, C. Jacoby, S. Burghoff, B.A. French, J. Schrader, U. Flögel, Early assessment of pulmonary inflammation by 19F MRI in vivo, *Circ. Cardiovasc. Imaging* 3 (2010) 202–210, <https://doi.org/10.1161/CIRCIMAGING.109.902312>.
 - [52] U. Flögel, S. Su, I. Kreideweiss, Z. Ding, L. Galbarz, J. Fu, C. Jacoby, O. Witzke, J. Schrader, Noninvasive detection of graft rejection by in vivo (19F) MRI in the early stage, *Am. J. Transplant.* 11 (2011) 235–244, <https://doi.org/10.1111/j.1600-6143.2010.03372.x>.
 - [53] C. Jacoby, N. Borg, P. Heusch, M. Sauter, F. Bönner, R. Kandolf, K. Klingel, J. Schrader, U. Flögel, Visualization of immune cell infiltration in experimental viral myocarditis by (19F) MRI in vivo, *Magma* 27 (2014) 101–106, <https://doi.org/10.1007/s10334-013-0391-6>.
 - [54] F. Bönner, C. Jacoby, S. Temme, N. Borg, Z. Ding, J. Schrader, U. Flögel, Multifunctional MR monitoring of the healing process after myocardial infarction, *Basic Res. Cardiol.* 109 (2014) 430, <https://doi.org/10.1007/s00395-014-0430-0>.
 - [55] S. Temme, C. Grapentin, C. Quast, C. Jacoby, M. Grandoch, Z. Ding, C. Owenier, F. Mayenfels, J.W. Fischer, R. Schubert, J. Schrader, U. Flögel, Noninvasive imaging of early venous thrombosis by 19F magnetic resonance imaging with targeted perfluorocarbon nanoemulsions, *Circulation* 131 (2015) 1405–1414, <https://doi.org/10.1161/CIRCULATIONAHA.114.010962>.
 - [56] A. Göpferich, Mechanisms of polymer degradation and erosion, *Biomaterials* 17 (1996) 103–114, [https://doi.org/10.1016/0142-9612\(96\)85755-3](https://doi.org/10.1016/0142-9612(96)85755-3).
 - [57] O. Koshkina, P.B. White, A.H.J. Staal, R. Schweins, E. Swider, I. Tirota, P. Tinnemans, R. Fokkink, A. Veltien, N.K. van Riessen, E.R.H. van Eck, A. Heerschap, P. Metrangola, F. Baldelli Bombelli, M. Srinivas, Nanoparticles for "two color" 19F magnetic resonance imaging: towards combined imaging of biodistribution and degradation, *J. Colloid Interface Sci.* 565 (2020) 278–287, <https://doi.org/10.1016/j.jcis.2019.12.083>.

- [58] D.R. Spahn, Blood substitutes Artificial oxygen carriers: perfluorocarbon emulsions, *Crit. Care* 3 (1999), <https://doi.org/10.1186/cc364>.
- [59] Y. Tsuda, K. Yamanouchi, K. Yokoyama, T. Suyama, M. Watanabe, H. Ohyanagi, Y. Saitoh, Discussion and considerations for the excretion mechanism of perfluorochemical emulsion, *Biomater. Artif. Cells Artif. Organs* 16 (1988) 473–483, <https://doi.org/10.3109/10731198809132602>.
- [60] A.R. Burgan, W.C. Herrick, D.M. Long, D.C. Long, Acute and subacute toxicity of 100% PFOB emulsion, *Biomater. Artif. Cells Artif. Organs* 16 (1988) 681–682, <https://doi.org/10.3109/10731198809132638>.
- [61] E. Lartigau, C. Thomas, M. Le Blanc, J. Riess, D. Long, C. Long, E.P. Malaise, M. Guichard, New high O₂ carrying perfluorochemical emulsions: toxicity, radiosensitivity of GM-CFC and development of metastases in mice, *Int. J. Radiat. Oncol.* 16 (1989) 1153–1156, [https://doi.org/10.1016/0360-3016\(89\)90272-1](https://doi.org/10.1016/0360-3016(89)90272-1).
- [62] A. Gálisová, V. Herynek, E. Swider, E. Sticová, A. Pátiková, L. Kosinová, J. Kríž, M. Hájek, M. Srinivas, D. Jiráček, A trimodal imaging platform for tracking viable transplanted pancreatic islets in vivo: F-19 MR, fluorescence, and bioluminescence imaging, *Mol. Imag. Biol.* (2018), <https://doi.org/10.1007/s11307-018-1270-3>.
- [63] C. Constantinides, E. McNeill, R. Carnicer, A. Al Haj Zen, R. Sainz-Urruela, A. Shaw, J. Patel, E. Swider, R. Alonaizan, L. Potamiti, A. Hadjisavvas, S. Padilla-Parra, K. Kyriacou, M. Srinivas, C.A. Carr, Improved cellular uptake of perfluorocarbon nanoparticles for in vivo murine cardiac 19F MRS/MRI and temporal tracking of progenitor cells, *Nanomed. Nanotechnol. Biol. Med.* (2018), <https://doi.org/10.1016/j.nano.2018.10.014>.
- [64] M. Longmire, P.L. Choyke, H. Kobayashi, Clearance properties of nano-sized particles and molecules as imaging agents: considerations and caveats, *Nanomedicine* 3 (2008) 703–717, <https://doi.org/10.2217/17435889.3.5.703>.
- [65] J. Bourquin, A. Milosevic, D. Hauser, R. Lehner, F. Blank, A. Petri-Fink, B. Rothen-Rutishauser, Biodistribution, clearance, and long-term fate of clinically relevant nanomaterials, *Adv. Mater.* 30 (2018) 1704307, <https://doi.org/10.1002/adma.201704307>.
- [66] P. Boehm-Sturm, L. Mengler, S. Wecker, M. Hoehn, T. Kallur, In vivo tracking of human neural stem cells with 19F magnetic resonance imaging, *PLoS One* 6 (2011), e29040, <https://doi.org/10.1371/journal.pone.0029040>.
- [67] M. Krekorian, G.O. Fruehwirth, M. Srinivas, C.G. Figdor, S. Heskamp, T.H. Witney, E.H.J.G. Aarntzen, Imaging of T-cells and their responses during anti-cancer immunotherapy, *Theranostics* 9 (2019) 7924–7947, <https://doi.org/10.7150/thno.37924>.
- [68] M. Srinivas, P. Boehm-Sturm, M. Aswendt, E.D. Pracht, C.G. Figdor, I.J. de Vries, M. Hoehn, In vivo 19F MRI for cell tracking, *JoVE* (2013), e50802, <https://doi.org/10.3791/50802>.
- [69] H. Zhang, S. Bo, K. Zeng, J. Wang, Y. Li, Z. Yang, X. Zhou, S. Chen, Z.-X. Jiang, Fluorinated porphyrin-based theranostics for dual imaging and chemophotodynamic therapy, *J. Mater. Chem. B* 8 (2020) 4469–4474, <https://doi.org/10.1039/D0TB00083C>.
- [70] Y. Zhang, S. Bo, T. Feng, X. Qin, Y. Wan, S. Jiang, C. Li, J. Lin, T. Wang, X. Zhou, Z. Jiang, P. Huang, A versatile theranostic nanoemulsion for architecture-dependent multimodal imaging and dually augmented photodynamic therapy, *Adv. Mater.* 31 (2019) 1806444, <https://doi.org/10.1002/adma.201806444>.